WIND ENERGY
Wind Energ. 2015; **00**:1–17
DOI: 10.1002/we

RESEARCH ARTICLE

Performance evaluation of a floating lidar buoy in nearshore conditions.

Miguel A. Gutiérrez-Antuñano[1], Jordi Tiana-Alsina[1] and Francesc Rocadenbosch[1,2]

[1] Dept. of Signal Theory and Communications (TSC), Remote Sensing Lab. (RSLab), Universitat Politècnica de Catalunya (UPC), Campus Nord, C/ Jordi Girona 1-3, 08034 Barcelona, Spain
[2] Institut d'Estudis Espacials de Catalunya (IEEC), Campus Nord, C/ Jordi Girona 1-3, 08034 Barcelona, Spain

ABSTRACT

This work provides a signal-processing and statistical-error analysis methodology to assess Key Performance Indicators for a floating Doppler wind lidar. The study introduces the raw-to-clean data processing chain, error assessment indicators and Key Performance Indicators, as well as two filtering methods at post-processing level to alleviate the impact of angular motion and spatial variability of the wind flow on the performance indicators. Towards this aim, the study mainly revisits Horizontal Wind Speed and Turbulence Intensity measurements with a floating ZephIR 300 lidar buoy during a 38-day nearshore test campaign in Pont del Petroli (Barcelona). Typical day cases along with overall statistics for the whole campaign are discussed to illustrate the methodology and processing tools developed.

KEYWORDS

Doppler wind lidar; Offshore wind farm; Resource assessment; Turbulence; Signal processing

Received . . .

1. INTRODUCTION

Over the past few decades, offshore wind turbines have started to exploit the energy from strong, homogeneous wind fields found over the oceans. Regardless that offshore wind farms are being operated in shallow and deep waters, specially in Europe [1] [2], the associated costs are still higher than for onshore wind farms. Therefore, one of the key challenges associated with the offshore wind industry is to obtain reliable cost-effective wind-speed measurements without the high project timescales of an offshore met mast.

Concerning assessment and planning of candidate wind farm locations, there are diverse ways of gathering wind-data information in offshore locations such as met masts [3], satellites [4][5], numerical models [6], and ground-based radar [7], each one with its own advantages and disadvantages. However, lidars are now being accepted as the best suitable *remote sensing technology* for offshore wind farms [8][9][10][11]. When wind lidars are placed over floating offshore platforms, like buoys, they permit to measure winds without resorting to expensive equipment like wind-monitoring towers or , satellite sensors (with comparatively lower spatial resolution), or numerical simulations [12][13]. Additionally, remote sensing devices such as floating wind Doppler lidars enable to evaluate the wind resource in a larger area since they are more versatile and can easily be redeployed [11].

Sea-waves induced motion degrade the wind vector measured by floating lidar devices [14][15] as well as the measured atmospheric turbulence. The latter impacts wind energy in several ways, specifically through power performance effects, turbine loads, fatigue and wake effects, and noise propagation. Therefore, motion compensation solutions to minimize the effects of motion on the lidar-measured wind speeds (e.g., through post-processing algorithms) or the movement of the lidar system itself (e.g., through mechanical compensation or by using ad-hoc floating platforms) become necessary.

So far, two main approaches have been adopted by system providers [16] when choosing the type of floating platform to be used: The first one consists of placing the lidar device on a platform able to absorb the motion of the sea in order to provide the necessary stability, and hence, to guarantee reliable wind-data measurements[17]. These platforms are typically

Prepared using weauth.cls [Version: 2010/06/17 v1.00]

either a *spar buoy* or a tension leg buoy [17]. The main disadvantage of these kind of buoys is that they are expensive and difficult to deploy. The second approach consists of using a *wave buoy* [18]. However, the main consequence of the small size associated to this typology of buoys is that they suffer from translational and rotational motion, all of which has to be mechanically or software compensated. Translational motions (i.e., sway, surge, and heave, corresponding to movements along the x, y and z axes, respectively) can easily be compensated by subtracting the motion vector from the measured wind vector while rotational motion (roll, pitch, and yaw, corresponding to rotational motions around the x, y and z axes, respectively) are more difficult to cancel out. Buoy tilting has a strong impact on lidar LoS measurements and, therefore, it can induce biases on the measured wind vector [19]. Two motion-compensation approaches can be outlined, which are potentially significant issues in the roadmap for the commercial acceptance of floating lidar technology [20]:

On one hand, in [21] the authors have placed the lidar on a 3-m diameter floating platform equipped with a *mechanical motion-compensation frame* to reduce the impact of lidar motion on the measured wind speed. A cardanic frame, which keeps the lidar virtually stand still and pointing to the zenith, was proposed and optimized. Lab-based harmonic oscillatory motion tests were carried out to assess solution performance and to show that signal fluctuations induced by periodic tilting of the buoy can virtually be removed under a wide range of cases (i.e., different tilting amplitudes and periods). It has been shown that angular motion is the main error source [19] [22].

On the other hand, one could try to reduce motion-induced errors by recording the buoy dynamics (i.e., its attitude) and by using *numerical algorithms* that help to correct the measured wind data. The residual uncorrected effects of such errors not only translates into additive noise to the measured wind signal but also as an "extra" turbulence [23]. To this end, here we show successful results from an original motion-compensation algorithm based on adaptive window averaging, which is analysed in both the temporal and spectral domains.

In this work, we discuss on the different error sources (e.g., motional versus turbulent) that degrade wind field measurements and we tackle spectral analysis [24] to validate the filtering methods applied, all of which is to contribute scientific novelty [25]. This is a vast field of research that has also given rise to a wealth of simulation studies with synthetic turbulent wind files in the state of the art [26] [27].

In accordance with recommended practice (Key Performance Indicators (KPIs) versus data availability) [20] and a growing maturity of floating lidars, a further contribution of this work concerns the methodological aspect with focus on the post-processing stage. Thus, departing from a 38-day nearshore campaign, system performance is assessed by using 1-s and 10-min time-series statistical analysis [24]. 1-s analysis (less usual in the state of the art) is to enable a better understanding of the involved phenomena, particularly, motion and turbulence.

This paper is structured as follows: Sect. 2 introduces the experimental set-up of the measurement campaign at El Pont del Petroli (PdP), Barcelona, involving a floating Doppler lidar (offshore) and a fixed reference lidar (onshore). Sect. 3 summarizes the raw-to-clean-data signal processing as well as the error assessment methodology used to assess the performance of floating lidar. Two filtering methods, motion-compensation and spatial-variation (SV) screening, are also presented. Sect. 4 tackles discussion results for the 38-day PdP campaign and the degree of fulfillment of KPIs when using the proposed methodology. Conclusion remarks are given in Sect. 5.

2. FIELD EXPERIMENT SET-UP

Wind measurements from two ZephIR 300 lidars were intercompared at PdP facilities (41°26'24.5760"N 2°14'56.5008"E, Badalona, Barcelona, Fig. 1a [28]. The physical environment consists of metropolitan low-rise buildings (typically, 20-m tall) along the coast line. The PdP area is part of the commuter belt of the city and the spatial organization of its settlements follows urban typology. One of the lidars was on a stand still configuration on land (i.e., the"reference" lidar), and the other was assembled on a buoy (i.e., the "moving" or "floating" lidar), as shown in Fig. 1b.

The fixed lidar was the key reference instrument used in PdP campaign. The lidar was directly rented to the manufacturer (ZephIR Lidar) and, as part of the Quality Assurance (QA) program, before and after PdP campaign it underwent QA tests against an IEC 61400-12-1-compliant met mast. Besides, both lidars (i.e., the "reference" and the "floating" one) were placed fixed on land 1-m apart during 3-h intercomparison periods before and after PdP campaign in order to verify identical measurements under 1-s and 10-min time basis. These tests were performed at the PdP pier so as to have topographical and environmental conditions as close as possible to those of the offshore campaign.

The ZephIR 300 is a continuous-wave (CW) focused Doppler lidar system specially adapted for offshore environments. It is widely used in the wind industry and has shown its trustability in deployments and verification processes to assess the quality of its data [29]. The system is able to profile the wind up to more than 200 m in height by using the Vertical Azimuth Display (VAD) scanning technique [30]. The lidar can measure at a user-defined set of heights between 10 m and 200 m in steps of 1 m. Due to the laser and optics characteristics of the lidar, it exhibits a height-dependent spatial resolution (e.g., 15 m when focusing at 100 m in height). The lidar achieves 1-s time resolution (when not refocusing) by using 50 Line-of-Sight (LoS) beams per second. It is worth noting that the measurement is not perfectly uniform (this point will be further discussed in Sect. 3.)

Wind Energ. 2015; **00**:1–17 © 2015 John Wiley & Sons, Ltd.
DOI: 10.1002/we
Prepared using weauth.cls

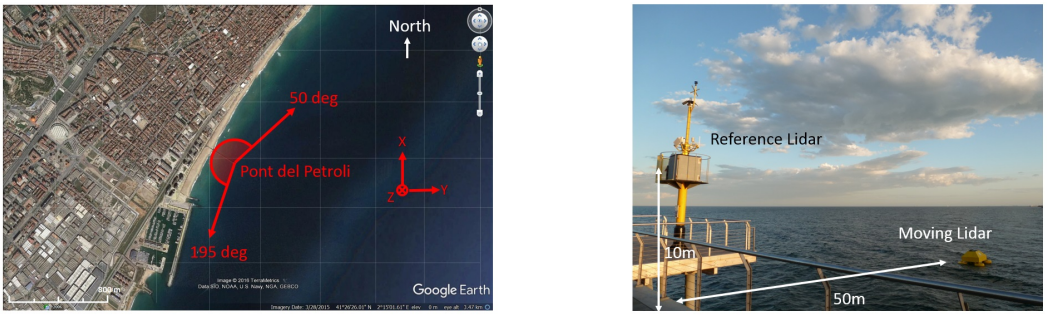

(a) (b)

Figure 1. PdP test campaign site. (a) Location of the test site near Barcelona coast. Red vectors along NE and SSW directions delimit the angles of the circular sector influenced by land. Fixed cartesian coordinate system used as part of the fixed reference frame is also shown. (b) Metereological tower and prototype lidar buoy.

PdP includes a full meteorological station mounted on a tower at the end of the pier including a NORTEK Aquadopp© underwater current meter (5 m depth), a SBE 37-SM C-T pressure sensor, a Vaisala HMP-155 temperature and humidity probe, a LP02 Young 52203 rainfall sensor, a Gill Instruments WindSonic anemometer, and a Vegapuls 62 radar-based sea-state and water-height measurement device. Webcams are also installed for both safety and beach-line monitoring. A WiFi link connects these sensors to an office computer on a nearby building and from there to the Internet, so that data gathered by all these instruments can easily be accessed, along with their performance, on a real-time basis. Because the buoy housing the ZephIR 300 lidar was a proof-of-concept custom-made system developed for this purpose, it was powered by a submarine electrical power cable connected to PdP which also sent data to a datalogger installed in the support tower in the dock. The buoy integrates the "floating" ZephIR 300 lidar as well as the two Inertial Measurement Units (IMUs) described in Sect. 3.1.

The PdP campaign extended from May 24th, 2013 to June 31st, 2013, i.e., during the late spring / early summer period. Weather at this time of the year is dominated by local thermal winds not going over 15 m/s speeds at 100 m in height although occasional episodes of terrestrial wind blowing from the north may occur. Heavy eastern storms seldom happen to blow in early summer and, in fact, none did so during the campaign. During the campaign wind speeds ranged from 1 m/s to 15 m/s at 100 m in height (see Fig. 2a) with three predominant directions: from the South, from North East and from the North-West (see Fig. 2b). Typically, during the night, there is light land breeze (3-4 m/s) blowing from land to sea (WNW direction in Fig. 2b) and characterised by more turbulent behaviour than day wind. During the day, there is usually sea breeze blowing from sea towards land (NE and SSW directions in Fig. 2b) of higher intensity (4-7 m/s) and lower turbulence (see also Fig. 3a). The average wind blowing pattern along with the lidar-observed SV over the 38-day campaign is shown in Fig. 3. Because Fig. 3c represents the 38-day average wind direction (WD), when Fig. 3c is compared to Fig. 2b the reader will notice that the 300-deg WD in Fig. 3c between approximately 0-5h UTC corresponds to the WNW direction in the wind rose of Fig. 2b. In contrast, the rough 120-deg WD for 7-20 h UTC time interval corresponds to the average of NE ($\approx$ 50 deg) and SSW ($\approx$ 195 deg) wind directions in Fig. 2b.

Concerning atmospheric stability, [31] came up with classification thresholds interrelating stability parameters (e.g., Turbulence Intensity (TI), turbulent kinetic energy (TKE) and the like) and stability class conditions. From this background and using that, for this site, the lidar-observed SV parameter is well correlated with the lidar-observed TI (this assertion will be further discussed in Sect. 3.2 and Fig. 5), it emerges from (Fig. 5a) that for this site low SVs (SV $\approx$ 0.02 roughly related to TI $\approx 5\%$) are associated to stable conditions while high SVs (SV $\approx$ 0.05 related to TI $\approx 15\%$) are are associated to convective ones. No fog or low-cloud events occurred during the campaign.

3. ASSESSMENT METHODOLOGY AND DATA PROCESSING

The methodology and signal processing tools aim at cross-examining wind-measured data from the "reference" lidar and the "floating" lidar previously introduced. Aim is to statistically describe and quantify motion-induced error on the retrieved wind parameters, namely, HWS, Wind Direction, and TI. Fig. 4 block diagram summarises the post-processing steps used in this approach, from level 0 (1-s data) to level 2 (post-processed motion-compensated data).

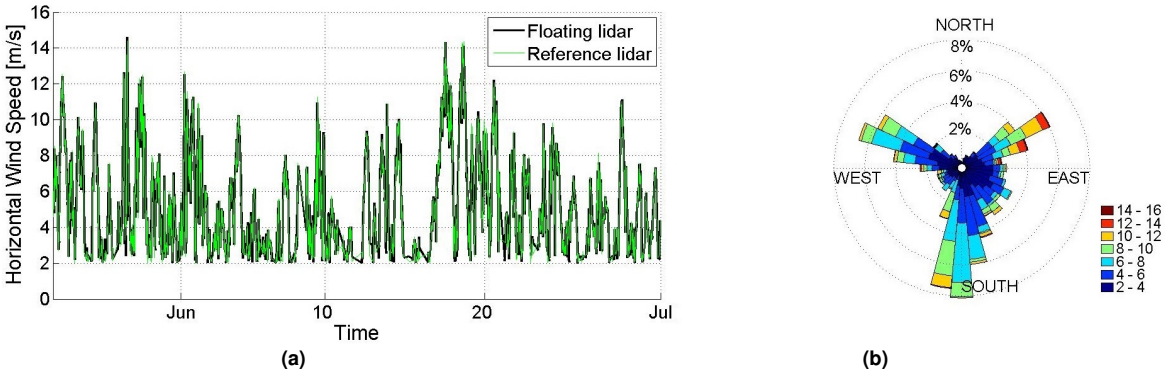

Figure 2. HWS time series and synoptic description of the wind flow at the test site during PdP campaign at 100 m in height. (a) 10-min HWS time series. (b) Wind rose showing 10-min WD bins for the reference lidar. Wind speeds below 2 m/s have been removed according to outliers' criteria [20].

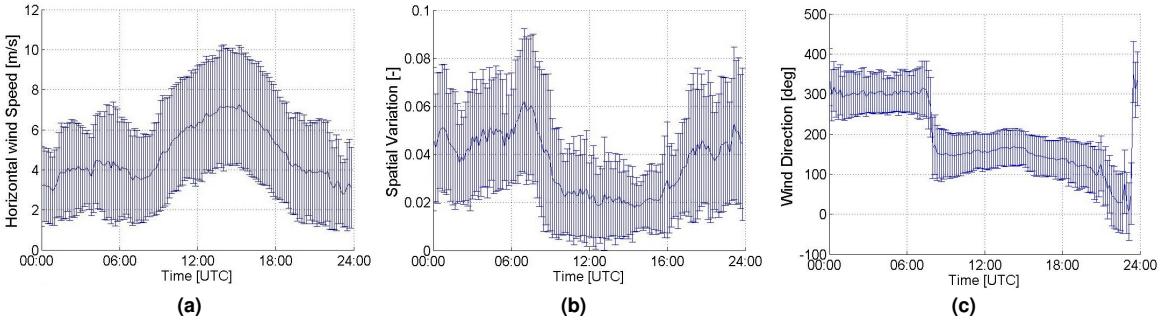

Figure 3. 38-day average wind patterns during the daily cicle. (a) HWS, (b) SV and (c) WD. Note: Time is UTC. Errorbars are computed at 1σ from 10-min data.

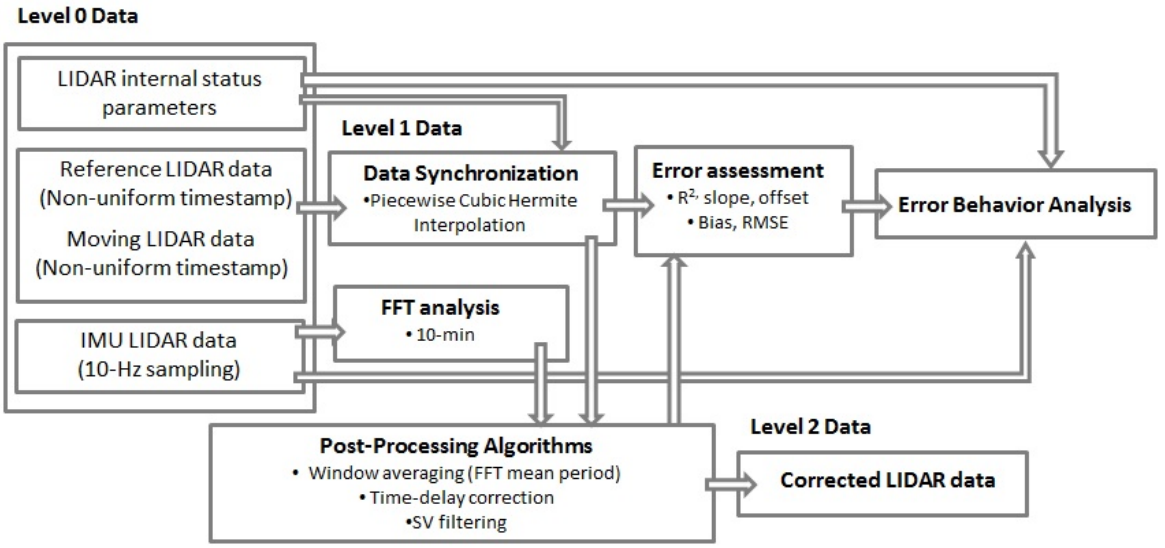

Figure 4. Wind lidar signal-processing block diagram.

Wind Energ. 2015; **00**:1–17 © 2015 John Wiley & Sons, Ltd.
DOI: 10.1002/we
Prepared using weauth.cls

3.1. From level-0 to level-1 data

Raw data.- Raw data comprises: (i) wind-lidar data from the Doppler lidar instrument, (ii) lidar internal status parameters and (iii) "floating" lidar motion time series gathered by the IMUs. Wind-lidar data includes HWS, WD, Vertical Wind Speed (VWS) as well as the lidar-observed TI.

TI magnitude highly depends on the location, the fetch, the measurement height and HWS, but typical values of horizontal TI, measured in offshore wind farm locations at 50-m heigth and above 10 m/s HWS, are around 8% to 10% [32]. An important remark to be mentioned here is that the *lidar-observed* TI figure is not completely equivalent to the *true*-TI measured by point-like ultrasonic or cup anemometers. This is due to the fact that the lidar-observed TI is affected by the inherent spatial and temporal averaging of the measuring instrument, which is directly linked to the spatial and temporal resolution window of the instrument [33][34]. Thus, in the case of the CW ZephIR 300, the measurement at a given height requires focusing the lidar beam at that height, which means that the instrument measures the average of the ensemble of radial velocities in the sounding volume determined by the laser beam and a probe length equal to the depth of focus (the probe length increases with the square of the focus distance). A similar and second-order effect is due to the conical scanning mechanism and related wind-component retrieval algorithm (VAD), which causes a portion of the scanning circle to be spatially averaged. These volume averaging effects cause that the lidar filters out turbulent scales smaller than the probe length and that it estimates standard deviations about 80% of the true value measured by cups in flat terrain [34]. Differences between the lidar-observed and the true wind spectrum will be discussed in Sect. 4.3.

Lidar internal status parameters are also part of the raw data available and they are used to assess wind data. These status parameters are the SV, the backscatter (i.e., the intensity of the attenuated backscattered light return), and secondary system parameters. The SV parameter, also called turbulence parameter (TP), has been considered "black box" insofar as it is related to the TI, which justifies the SV-TI correlation study conducted in Sect. 3.2 next.

IMU data enables to track the "floating" lidar attitude. We have used a Microstrain 3DM-GX3-45 IMU equipped with a GPS antenna. Attitude data includes Euler angles (roll, pitch and yaw), which describe lidar system orientation with respect to a fixed-coordinate system (see Fig. 1a), translational accelerations on these axes, and GPS position of the buoy. IMU acquisition frequency can be adjusted between 1-10 Hz to match that of the wind lidar data.

The above lidar-related variables are acquired at 100 m in height and at two different time resolutions, 1-s and 10-min (except for the TI which is calculated every 10-min from 1-s datasets). 10-min is the usual time basis used in the wind industry, while the 1-s time basis is used here to better understand error behaviour and its compensation. 10-min data availability was 100% for the reference lidar and 99.98% for the floating lidar. After eliminating outliers - as signaled by lidar internal status parameters (999X labels, too high wind speeds, rain, etc.) - data availability became approximately 90% for both lidars. Rejection percentage due to external parameters was around 15% due to low wind speeds.

Data synchronization and time-delay correction.- The ZephIR 300 lidar acquires and outputs data under a non-uniform time basis close to 1 s. Because of internal system protocols (e.g., cloud averaging and refocusing actions) the output data stream at one particular height may contain time gaps of several seconds and a non-uniform sampling period roughly between 1 and 5 s. First, *data synchronization* becomes necessary to compose and intercompare wind-related data streams (e.g., HWS, WD, pitch and roll) from the two different lidars. This is accomplished by first creating a master time vector with a uniform timestamp common to all the sensors involved (mainly the two lidars and the IMUs). Towards this end, 1-s linear and piece-wise cubic Hermite interpolation methods [35] have been used to resample the time vector of all the sensors into the common time vector. For both methods, identical results have been obtained in the statistics of Section 4. Time gaps equal to or larger than 10-s have been marked as "signal drop outs" in the master time vector when computing statistics. Second, a *time-delay correction* is necessary to intercompare wind lidar data (e.g., HWS) from the two lidars separated a given distance. The time delay is estimated by standard cross-correlation analysis of the time delayed signals (i.e., the time shift yielding maximum correlation between the "floating" and the "reference" signals). The underlying principle here is Taylor's frozen-atmosphere hypothesis [35], which states that turbulent eddies transported by the mean wind flow do not change their properties as if they were frozen.

By applying this raw data processing methodology to the wind data measured by both the "floating" and the "reference" lidar, level-1 data (clean data) is obtained and the HWS time series measured by the two lidars can readily be intercompared.

3.2. Error assessment

Main indicators.- Main indicators used to assess performance when comparing wind variables measured simultaneously from both lidars (i.e., by the "fixed" or "reference" lidar and by the "moving" or "floating" lidar) are inherited from classic statistics. These indicators are: (i) *Bias* (i.e., the difference between the value of a wind variable measured by the "floating" lidar and the true value measured by the "reference" lidar), (ii) RMSE, i.e., the square root of the mean square error (MSE)), and (iii) *scatter-plot analysis*. Concerning scatter-plot analysis, three parameters related to the linear fit between v_{moving} and v_{ref} are computed to assess their correlation degree: slope and offset of the straight line fit and the coefficient of determination, ρ^2. Two linear-regression models, with and without offset term ($y = ax + b$ and $y = ax$, respectively) have been considered.

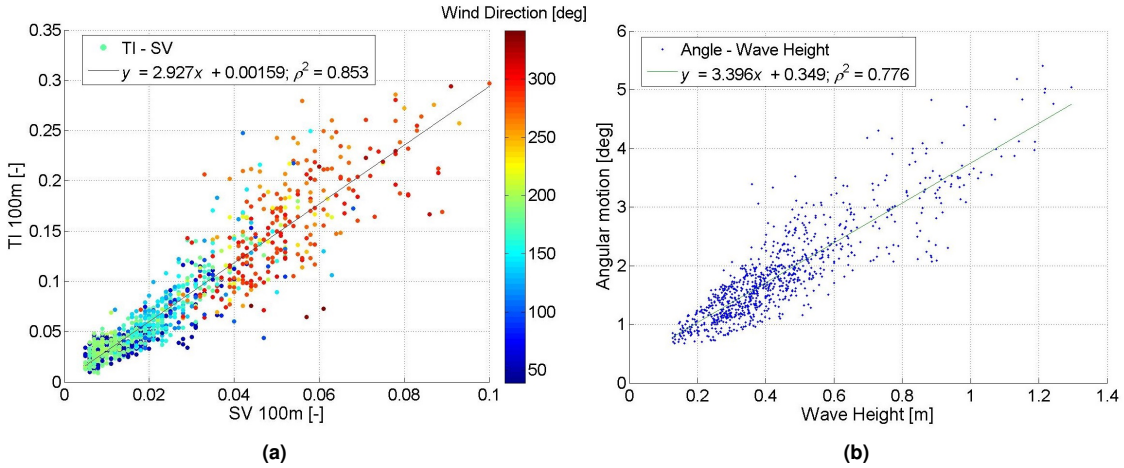

Figure 5. (a) Scatter plot showing SV-TI correlation (100-m in height). Each dot represents 10-min data computed from the available 38-day 1-s PdP-campaign dataset. Dots are color-coded according to WD. (b) Scatter plot showing the correlation between the wave height and buoy angular-motion parameter, $AM = \sqrt{\alpha^2 + \beta^2}$ [deg RMS]. Wave height has been measured hourly. Angular motion has been computed hourly from IMU data by averaging six 10-min RMS samples every hour.

The above indicators are linked to confidence thresholds, which provide acceptance criteria for both the HWS and the WD measured. These two variables are considered key ones in the wind industry on a 10-min basis [20].

As it can be seen from Tab. I, acceptance criteria depend on the time resolution (1 s or 10 min) of the acquired data. While 10-min criteria come from [20], 1-s criteria come from the authors under the general guideline that acceptance criteria under 10-min average interval must obviously be more stringent than under 1-s average. For 10-min data an asterisk indicates that the general guideline of a $2-4\%$ uncertainty for commercial systems (Tab. I summary roadmap in [20]) is considered.

Two off-the-shelf variables have been used to aid the error assessment study: SV and the so-called angular-motion parameter. The former is related to the lidar-observed TI, the latter to the buoy angular motion. They are explained next:

On the SV-TI correlation.- The so-called TP or SV parameter represents the variation degree -turbulence- of the radial wind speeds (LoS) within the circle of scan [34]. Following [34], the SV parameter is defined as the turbulence intensity of the radial wind speed over one rotation of the conically scanning lidar (see Eq. (12) therein). From a statistical point of view, it may be understood as an indicator of the goodness of the VAD fitting of the radial velocities within the scanning circle used to retrieve the estimated wind vector at a given height.

In order to closely study the SV-TI at one particular height (100 m here) an empirical SV-TI correlation study has been carried out by using 1002, 10-min measurements from the whole PdP campaign. To enhance the representativeness of the statistical sample, each measurement was chosen by ensuring that all other measurements within a 1-h window centered on the sample measurement (i.e., sample measurement ± 30 min) were also compliant with outliers' criteria [20] and the lidar's manufacturer reliability specification (basically, HWS $\geq$ 2 m/s and exclusion of 999X labels). The lidar-observed TI has been computed over 10-min intervals and (SV, TI) pairs have been color-coded according to WD. Fig. 5a clearly shows that these two parameters are highly correlated (determination coefficient, $\rho^2 = 0.853$). Closer inspection of Fig. 5a reveals that mid-to-high values (i.e., (SV, TI) pairs above the (0.035, 0.1) point, shown by orange-reddish dots) are linked to WDs $\approx$ 270-300 deg. These WDs correspond to winds coming from the urban area (land breeze, Fig. 1a), which is consequent with higher terrain roughness due to the settlement of buildings along the coastline [36].

On angular-motion parameter.- In this work angular motion (AM) parameter is a buoy-related parameter defined as the RMS of the pitch and roll angular amplitudes ($AM = \sqrt{\alpha^2 + \beta^2}$, where α is the pitch RMS angular amplitude and β is the roll one). The angular-motion parameter correlates well with the *wave height* as shown by a determination coefficient, $\rho^2 = 0.776$, in Fig. 5b. Selection of the angular-motion parameter as one of our primary variable of study instead of wave height (which is traditionally used as a key parameter to assess candidate wind-farm locations) is motivated by three main reasons: (i) availability of the angular-motion parameter with a much higher temporal resolution (10-Hz IMU sampling rate, i.e., 100-ms resolution) than the wave height (1-h resolution from the wave-height sensor); (ii) the fact that the angular-motion parameter is a direct measurement of the buoy motion (via pitch and roll angles) and hence, of the floating lidar motion; (iii) the availability of pitch and roll angles as individual time series from the IMUs, which enables a more in-depth knowledge of the buoy's temporal motion and in relation to WD.

Wind Energ. 2015; **00**:1–17 © 2015 John Wiley & Sons, Ltd.
DOI: 10.1002/we
Prepared using weauth.cls

3.3. Filtering methods

Motion-compensation algorithms.- In order to reduce the impact of sea-induced angular motion (pitch/rool) on the retrieved wind speed measured by the floating lidar, motion compensation at post-processing level becomes necessary [22] [37]. Fig. 6a shows the 1-s HWS measured with the floating lidar (blue dots) and that of the reference lidar (black trace). While the HWS standard deviation for the reference lidar is $\sigma_{ref} = 0.36$ m/s over a 24-h period starting on June 18th, 2013, the standard deviation for the floating lidar becomes as high as $\sigma_{float} = 0.74$ m/s. Two motion-compensation approaches can be considered depending on whether LoS data is available or not to the correction procedure:

LoS correction.- This procedure takes advantage of the fact that the VAD algorithm combines multiple LoS to estimate the wind-speed components ((u, v, w), being each one the proyection of the wind vector along the x, y and z axis, respectively). Thus, in the case of the ZephIR lidar, 50 LoS are combined in each conical scan at a frequency of 1 scan/s. It is possible to deconvolve lidar motion in the radial velocity measured along each LoS by using Euler-angle formulations [38] and given attitude time series data (pitch and roll information). Because the geometry of the problem is known for each scanning LoS, the problem is invertible. From the point of view of its practical implementation this approach implies the prerequisite of individual LoS data being available [39].

Window averaging.- When LoS data is not available, as is our case, a most suitable correction strategy consists of filtering out motion-induced signal fluctuations recorded under 1-s time basis (see Fig. 6a). Window averaging is a class of low-pass filtering (or smoothing) techniques (Sect. 3) inherited from the Signal-Processing field [ref Proakis] that enable to filter out unwanted high-frequency components on the measured HWS such as those caused by motion of the floating lidar.

In this work, we propose *adaptive window averaging* of the HWS as motion-compensation algorithm. This straightforward post-processing technique relies on a simple boxcar low-pass filter of adaptive length that enables to filter out unwanted high-frequency components such as those caused by the motion of the floating lidar. The time window length is chosen to be the mean oscillatory period of the buoy/platform, which is estimated by Fast Fourier Transform (FFT) of the buoy angular motion measured by the IMUs (Fig. 6b) and recomputed every 10 minutes. Thus, each FFT is computed by using 6000, 10-Hz time-spaced samples (10-min time segment) and zero padding until reaching 8192 samples (nearest power of two, 2^{13}). From Fig. 6b (11:20 to 11:30 time segment) the motional behaviour of the buoy is dominated by a pitch-angle peak frequency, f = 0.25 Hz. Thus, it corresponds to a mean oscillatory period (window length) equal to T = 1 / 0.25 = 4 s. Fig. 6a illustrates application of this FFT-based window averaging from the temporal point of view (time-series processing). It is evidenced that once the window-averaging algorithm is applied to the floating lidar HWS signal (blue dots) random fluctuations significantly reduce and hence, the "floating" lidar HWS signal (red dots) becomes closer to the reference-lidar HWS (black trace). Analogous behaviour is reencountered from the spectral point of view (this is amply discussed in Sect. 4.3 in the context of wind spectrum analysis).

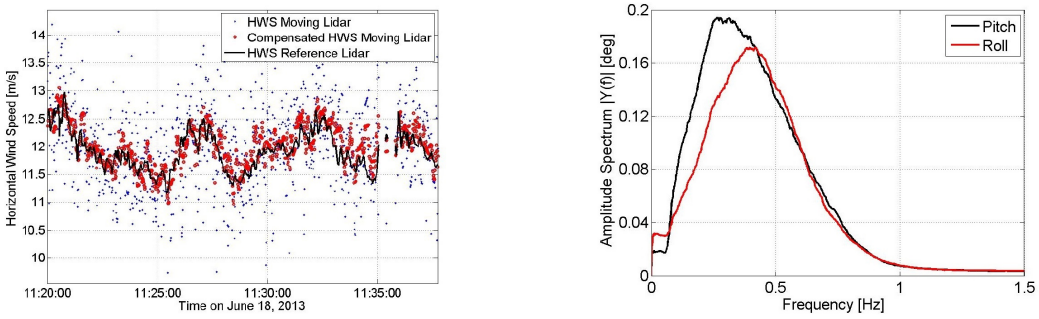

Figure 6. The adaptive window-averaging algorithm: (a) 1-s HWS time series measured by the "reference" lidar (black trace) and by the "floating" lidar (blue dots). 1-s HWS after window averaging (red trace). (b) Pitch and roll FFT of the buoy angular motion computed from the 10-min time segment starting at 11:20 and showing peak-dominant oscillatory behaviour at at peak frequency, f = 0.25 Hz.

SV filtering.- As introduced above, the SV parameter represents the wind variability in the scanning area. Coast-line terrain complexity nearshore the test site plays a non-negligible role in the variability of the wind flow at PdP. This is to say that SV may well impair statistical confidence indicators between the two lidars even if the floating lidar did not move. Therefore, and as the second step to come up with SV-compensated data apt for fulfilling wind-energy industry requirements, a SV-threshold filtering is applied. Fig. 7a shows the 1-s SV histogram for two representative days corresponding to low- and high-SV scenarios. Fig. 7b depicts the SV for the whole PdP campaign computed with 10-min

data. In both panels the SV threshold (0.05 and 0.1, respectively) is used to remove HWS measurement samples above the threshold. The threshold used for 10-min data is in agreement with [40].

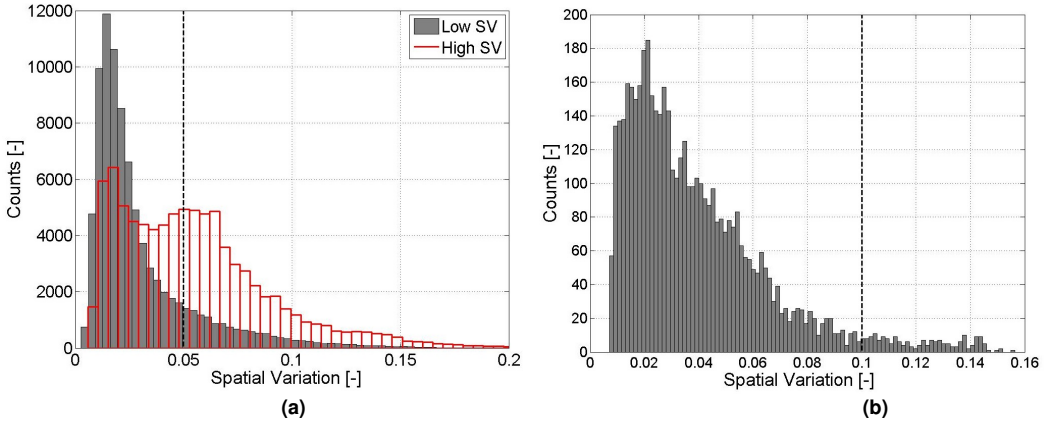

Figure 7. SV histograms. (a) Histogram of the SV distribution for two case examples (low- and high-SV scenarios) using 1-s data. (b) 10-min SV for the whole PdP campaign. (Both panels) dashed black lines indicate the screening threshold used.

4. DISCUSSION RESULTS

This Section is aimed at illustrating that the proposed assessment methodology of Sect. 3 is suitable for characterizing the HWS error behaviour of the floating lidar in terms of angular motion and lidar-observed wind turbulence (parameterized by the SV) as main error sources. Moreover, we present a summary statistical analysis for the whole 38-day PdP campaign, representative of the two filtering methods presented in Sec. 3.3, used to comply with the acceptance criteria and KPI indicators of Tab. I. Finally, and because of the importance of the TI for the wind industry, we show how the measurement reliability of the TI can be improved by application of Sect. 3 methods.

4.1. Quality of the reference lidar

Fig. 8 shows 1-s and 10-min HWS intercomparison tests before and after PdP campaign, when both lidar units where fixed. As mentioned in Sect. 2 both the "reference" and the "floating" lidar were placed fixed on PdP pier for these tests. Tests after PdP campaign yielded determination coefficients (ρ^2) and (straight-line fits) equal to 0.9960 ($y = 1.0065\,x + 0.0069\,[m/s]$) and 0.9990 ($y = 1.0094\,x + 0.0011\,[m/s]$) for 1-s and 10-min data, respectively. Likewise, RMSE were as low as 0.93% (1-s tests) and 0.04% (10-min tests). When the SV was intercompared (figure not shown), determination coefficient and straight-line fit were 0.9426 and $y = 0.9663\,x + 0.0004$ for 1-s data, and 0.9953 and $y = 0.9759\,x + 0.0003$ for 10-min data (intercomparison test before PdP campaign, virtually identical indicators after the campaign). Excellent agreement in the results above shows that the "floating" lidar remained calibrated during the entire measurement campaign.

4.2. On the impact of angular motion and SV on the retrieved HWS

In order to characterise the HWS error behaviour of the floating lidar, two case studies of statistical significance are discussed: *case 1* (Fig. 9) is representative of a high-angular-motion, low-SV scenario whereas *case 2* (Fig. 10) is representative of a low-angular-motion, high-SV scenario. At this point, we hypothesize that "low/high SV" accounts for SV primarily affected by patterns of the atmospheric conditions (atmospheric-induced SV due to e.g., low/high wind turbulence) and not that much - or secondarily - by patterns introduced by the motion of the floating lidar (motion-induced SV). To support this, the SV measured by the "reference" lidar has been compared against the SV measured by the "floating" lidar over the whole 38-day campaign (10-min data, statistical sample of 3937 points) in scatter-plot form (figure not shown). This has yielded a virtually ideal 1:1 correlation ($y = 1.065\,x$) with narrow dispersion ($\rho^2 = 0.948$) hence, showing that -because both lidars virtually measure the same SV- angular motion of the buoy has little effect on the lidar-observed SV. The physical explanation behind this result lies on the quasi-static behaviour of the buoy as compared to the conical scanning period of the lidar. Because typical oscillatory periods of the floating lidar buoy (3 to 5

DOI: 10.1002/we
Prepared using weauth.cls

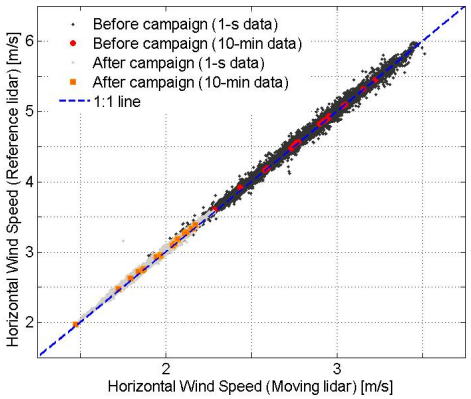

Figure 8. Example of HWS intercomparison tests before (02/05/2013 from 09:00UTC to 12:00UTC) and after (26/07/2013 from 09:30 to 12:30) PdP campaign using 1-s and 10-min data. Black and grey dots correspond to 1-s data before and after the campaign, respectively. Red and orange squares correspond to 10-min data.

s) are comparatively larger than the 1-s conical scanning period and angular amplitudes are usually lower than 15 deg, the floating lidar behaves as if it were apparently static for most of the scanning period.

Case 1 corresponds to a day (June 18th, 2013) with ENE (East-North East) wind (i.e., sea-to-land wind, see Fig. 1a), 8.0 m/s mean speed ("fresh breeze" in Beaufort scale) at 100 m in height while case 2 corresponds to a day (May 31th, 2013) with WNW (West-North-West) wind, 3.0 m/s mean speed ("light breeze") at 100 m in height. The "low motion" scenario is defined by a characteristic wave height between 0.1-0.5 m and $\approx$ 4 deg maximum angular amplitude while the "high motion" scenario is defined by a wave height between 0.5-1 m and $\approx$ 15 deg maximum angular amplitude. In both cases, Figs. 9-10 show the absolute error (magnitude of the difference between the value of a quantity measured by the floating lidar and its actual value given by the reference lidar) in the retrieved 1-s HWS as a function of the angular amplitude (Figs. 9a, 10a) and SV (Figs. 9b, 10b). Specifically, in Fig. 9 and 10, pitch (α) and roll (β) are calculated by averaging 10-Hz measurement every 1-s, while in Fig. 5b and 12 hourly and daily values are obtained by averaging the 10-min RMS values from 10-Hz measurements. Errorbars depict the approximate 1σ dispersion of the mean HWS error (Y-axis) and have been computed from the standard deviation in the retrieved mean absolute errors. Angular amplitudes have been grouped into 0.5-deg bins and SV into 0.01 bins when computing daily histograms for these two days.

Figs. 9a and 10a show that the HWS error can be bounded below 0.5 m/s when the motion amplitude is below 5 deg. This value is in agreement to previously published results [19] for low-to-mid wind speed (3-15 m/s). From a physical point of view, errors arise as a consequence of the inhomogeneous ensemble of turbulent- and motion-induced wind velocities (random variables) in the probe volume of the lidar. According to the central limit theorem stating that the probability density function (p.d.f.) of a myriad of independent random variables (no matter which their original distribution is) tends be Gaussian, one can assume errorbars do follow a Gaussian p.d.f. [41], which gives maximum likelihood of occurrence at the center of the errorbar (solid dots in Fig. 9 and 10). Under this assumption, when comparing Fig. 9a with Fig. 9b for case 1, it arises that when the angular amplitude is larger than approximately 5 deg the main contribution to the mean HWS error (tendency line shown in dashed black trace) comes from the lidar angular motion and not from the SV. This is also shown in Fig. 9b by HWS errors remaining bounded to approximately some 0.5 m/s for the whole SV range of the day, SV = 0-0.25. In contrast, in the low-motion scenario of case 2 (angular motion below 3.5 deg for the whole day, HWS error $<$ 0.4 m/s, Fig. 10a), the SV is the main error source (HWS error $>$ 0.4 m/s for SV $>$ 0.05, Fig. 10b), which accounts for the turbulent behaviour of the wind flow that day.

4.3. Wind spectrum analysis and motion compensation

Central to study the impact of sea-induced motion on the measured HWS and related performance of the motion-compensation algorithm (Sect. 3.3) is analysis of the HWS from a spectral perspective.

One-day-long 1-s HWS time series with an availability higher than 90% has been used to estimate the Power Spectral Density (PSD) for both the reference and the floating lidar under the two different motion scenarios presented above: "low motion" and "high motion". Three PSD estimators have been considered and intercompared: the periodogram, Welch's method and Burg's method [24] yet, in what follows, and because Burg's method yields exactly the same spectral estimates as Welch's but with a lower variance, all PSDs shown next are computed using Burg's. By experiment a filter order of M =

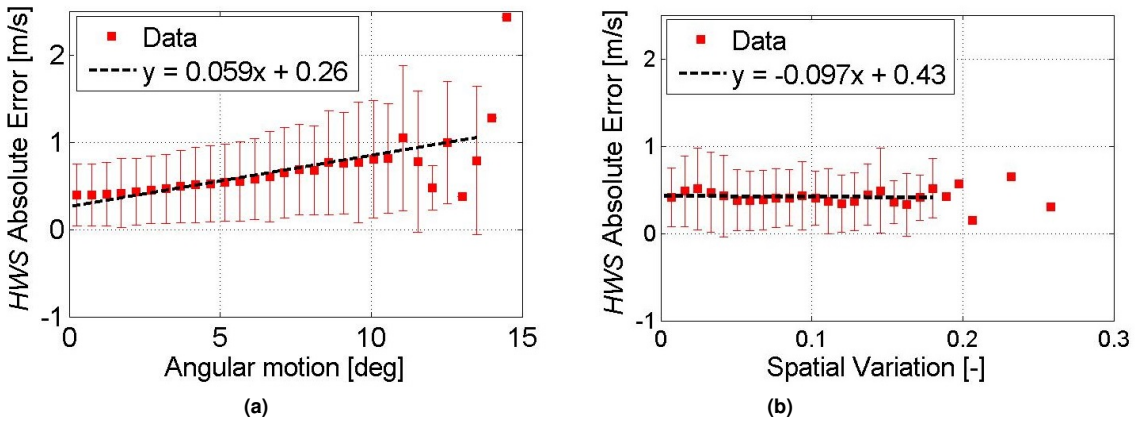

Figure 9. *Case 1*: High-angular-motion, low-SV case (June 18, 2013, 00:00-23:59 UTC). Behaviour of the mean 1-s HWS absolute error as a function of (a) angular motion amplitude (1 bin = 0.5 deg) and (b) SV (1 bin = 0.01 SV [a.u.]).

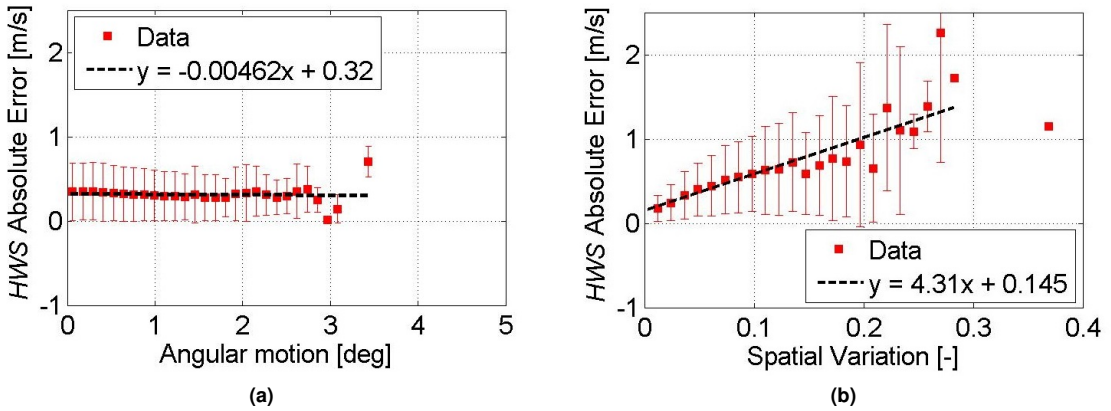

Figure 10. *Case 2*: Low-angular-motion, high-SV case (May 31, 2013, 00:00-23:59 UTC). (a-b) Same as Fig. 9.

1800 has been used in Brug's (this parameter being equivalent to using 6-h data segments, M' = 21600 samples in Welch's [42].

Fig. 11 shows the lidar-measured wind spectrum under low- (Fig. 11a) and high-motion (Fig. 11b) scenarios for (i) the reference lidar, (ii) the floating lidar, and (iii) the floating lidar after application of the motion-corrrection algorithm of Sect. 3.3. An assymptotic straight line has been fitted to the reference-lidar spectrum giving a fitting slope of -1.8, which is very close to the -5/3 theoretical slope - or "true" wind spectrum - ($\approx 8\%$ error) of Kolmogorov's spectrum function in the inertial range [43]. Important is also to notice the slight signal increase above the fitted assymptote or "true" wind spectrum in the frequency range between approximately $3\ 10^{-3}$ and $5\ 10^{-1}$ Hz observed by the floating lidar (this is better seen in the "low-motion" scenario of Fig. 11a). This is also in agreement with similar results in the state of the art [42]. When addressing the "high-motion" scenario of Fig. 11b, sea motion induces a strong increase in the spectral content from $2\ 10^{-3}$ to $5\ 10^{-1} Hz$ (end of the frequency range) of some $10\ dB$ at $f = 10^{-2} Hz$ and more that $15\ dB$ at $f = 5\ 10^{-1}\ Hz$ (blue trace). After applying the motion compensation algorithm of Sect. 3.3, the PSD of the floating lidar virtually coincides with that of the reference lidar, hence verifying the goodness of the proposed algorithm. The correction algorithm has been applied by recomputing the length of the adaptive tapering window every 10-min for the whole 24-h time series. Similar satisfactory results are obtained for the "low-motion" scenario, though with the added difficulty of having much lower spectral levels to correct.

4.4. PdP campaign statistical results

Fig. 12 summarises the 38-day campaign statistics on a daily basis using three different "filtering" stages from Sect. 3.3: (i) no filtering at all (red trace), (ii) motion compensation by window averaging (green trace), and (iii) window averaging

Wind Energ. 2015; **00**:1–17 © 2015 John Wiley & Sons, Ltd.
DOI: 10.1002/we
Prepared using weauth.cls

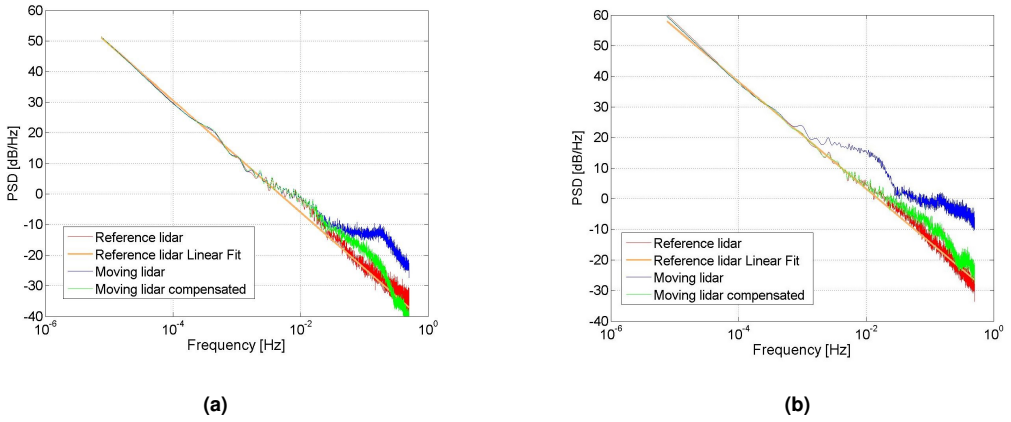

Figure 11. PSD of the lidar-measured HWS under low- and high-motion scenarios. (a) High-motion case showing wind spectra for the reference lidar (red), the floating lidar (blue), and the floating lidar after application of the motion-correction algorithm (green). (b) Low-motion case (same legend). The PSD is computed in units of $[(m/s)^2/Hz]$ and represented in decibels/Hz, $PSD\ [dB/Hz] = 10log_{10}\{PSD[(m/s)^2/Hz]\}$.

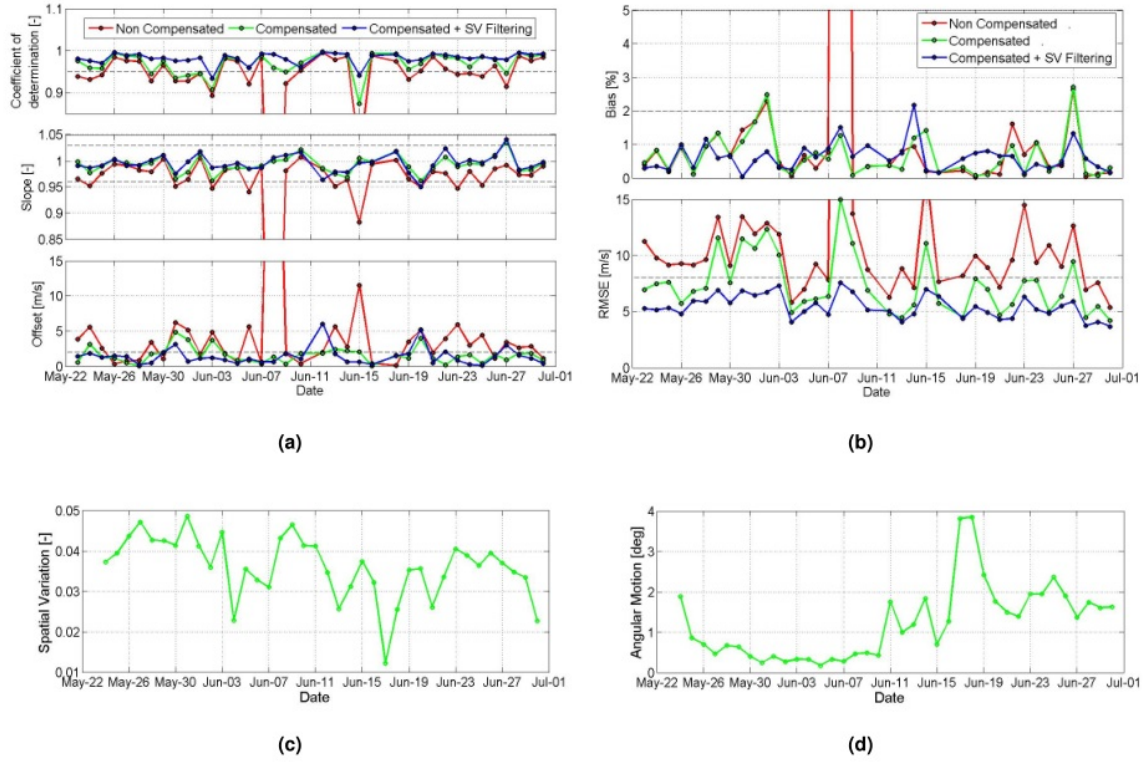

Figure 12. Performance statistics of 38-day PdP campaign using 1-s HWS data evaluated on a daily basis. (a) Linear fit regression indicators: coefficient of determination, ρ^2, slope, m, offset term, n. (b) Time-series statistical indicators: Bias, RMSE. Traces (all panels): (Horizontal dashed black) 1-s KPIs according to the range intervals given in Tab. I. (Red) No filtering method applied. (Green) Window averaging (Sect. 3.3). (Blue) Window averaging and SV filtering (Sect. 3.3). Each colored dot represents a measurement day with aggregated statistics. (c) Time-series external conditions: atmospheric-induced SV (Sect. 4.2) and (d) Angular motion (refer to Sect. 3.2). Note that all blue dots fulfil Tab. I KPI standards, i.e., they lie above the horizontal dashed black trace ((a), top panel), below it ((a), bottom panel; (b), both panels) or within dashed black traces ((a), middle panel).

plus SV filtering (blue trace). External conditions regarding the angular-motion parameter (Sect. 3.2) and the atmospheric-induced SV (Sect. 4.2) are also plotted as time series. For reference, the SV can be related to the lidar-observed TI via Fig. 5a and the angular motion can be related to the wave height via Fig. 5b. The adaptive window length of the motion-compensation algorithm has been computed by composing the 1-s time series for each day (86400 measurement samples) and by Fourier estimation of the buoy angular dominant period (peak level of the angular power spectrum distribution) every 10 minutes along the daily time series. The SV threshold (above which measurement samples are treated as outliers) has been set to SV $>$ 0.05 when computing daily histograms (38 histograms). This SV criterion yields a 30% mean rejection ratio over the 38-day measurement period for 1-s data. Though different SV thresholds can be set, there is always a trade-off between threshold level and data availability (i.e., the amount of "clean" data available for the end user after removing outliers).

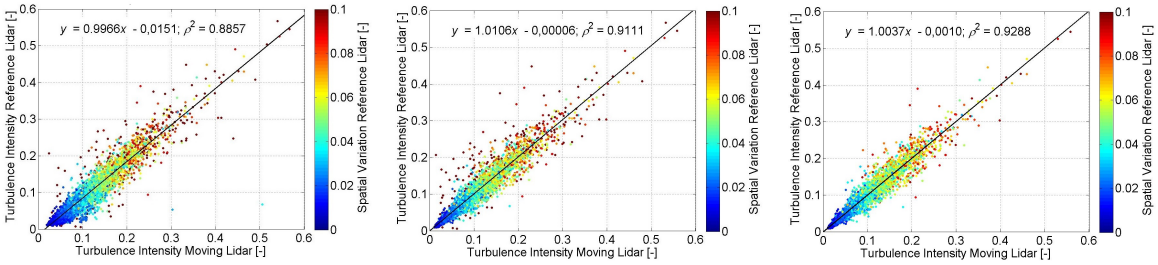

Figure 13. TI scatter plots for the whole campaign using 10-min data evaluated on for the whole campaign (May 23th, 00:00UTC, June 30th, 23:59UTC). (a) No filtering method applied (Red in Fig. 12). (b) After window averaging (Green in Fig. 12). (c) After window averaging and SV filtering (Blue in Fig. 12). (All plots) The colorbar codes SV.

Table II summarizes 1-s and 10-min KPI PdP-campaign error indicators for the three filtering stages considered ((i)-(iii) above) and in regard to HWS and TI variables. Statistics are representative of the whole PdP campaign and have been computed by using the composite 38-day time series. HWS case (ii) is skipped for 10-min data in Tab. II because typical FFT-window lengths for motion averaging are about 3 s, a much lower figure than 10 min. In brief, when 1-s data in Fig. 12 is cross-examined against Table I, it emerges that the window-averaging technique (case (ii) above) yields substantial improvement for most of the days, thus, raising the default 30% 1-s KPI compliance when no filtering procedure is applied (case (i)) to 80% compliance. In spite of the huge improvement given by the window-averaging technique, only after subsequent SV filtering (case (iii)) do we achieve that all days fulfil virtually all KPI requirements (98% compliance). When window averaging is used for motion compensation, the largest improvement in the error indicators of Tab. II occurs for the slope, which tends to the 1.000 ideality value (from 0.953 in case (i) to 0.993 in case (ii), 1-s data). The statistical indicator that behaves worse is the RMSE (from 12.24% in case (i) to 7.39% in case (ii), 1-s data).

These results warrant, however, some comments: Thus, day-by-day inspection of Fig. 12 reveals that in many days application of the motion-compensation algorithm is enough to ensure compliance of the 1-s KPIs of Tab. I (KPI's shown in horizontal dashed trace) and which outlines that deviations are mainly an effect of motion rather than of different atmospheric situations (mainly, turbulence). This is shown by a green trace (motion-compensated data) moving far apart from the orange trace ("no filtering at all") and virtually overlapping with the blue trace (motion compensation + SV filtering). Consider, for example, "coefficient of determination" in the top panel of Fig. 12a and refer to e.g., May, 24-25; Jun, 8-9; Jun. 19-23, 25-26, 28-30. On other days, SV filtering is the main responsible for ensuring KPI compliance, hence showing that the deviations are mainly an effect of the atmospheric situation. This is identified by virtually overlapping red and green traces and a blue trace moving far apart from them (in the same example above refer to e.g., May 29, 31; June 1-2, 24). On a few days, however, the dominant mechanism (angular motion or turbulence) is not so evident and deviations from KPI acceptance levels may well come from a combined effect of both (e.g., Jun. 15, 23 and 27).

A clear improvement in all statistical indicators is therefore observed, hence showing that the proposed methodology (that is, motion compensation by window averaging and SV filtering) is a suitable tool to improve the reliability of the data gathered by the floating lidar (98% compliance) while ensuring 70% data availability for the 1-s data and 95% data availability for the 10-min data (100% compliance).

4.5. TI results

As outlined in Sect. 1, atmospheric turbulence can have negative effects on power performance and reduce wind-turbine average lifetime. Therefore, reliable measurement of the TI becomes crucial for the wind industry. Differences between "real" (i.e., point-like measured) and "lidar-observed" TI (Sects. 3.1 and 4.3) can be problematic even for fixed lidar systems, not to mention for a moving lidar. Accepting these limitations for fixed lidars, in this subsection we show how successive application of the window-averaging and SV-filtering methods so far discussed aids to improve the reliability of the 10-min estimated TI by the floating lidar to a level *close* to that of the fixed lidar. First, 1-s data processing is forcibly used to enable application of the motion-compensation algorithm (Fig. 6a). Second, the output of this algorithm is recomposed into a 10-min time series from which a SV filter is applied and 10-min TI estimated (industry standard). Here, note that buoy motional periods typically range from three to a few seconds, which is a time scale according 1-s raw processing. Both lidars were well calibrated and located close enough so as to sense the same wind distribution and neglect instrumental errors (Sect. 4.1).

Fig. 13 shows TI scatter plots in response to the same signal processing cases discussed in the preceding subsection (cases (i), (ii) and (iii), in Sect. 4.4). To compute the scatter plots of Fig. 13 the 38-day campaign HWS data has been composed and synchronized (Sect. 3.1) into two 10-min time series (nominally, 5472 samples), one for the reference lidar and another for the floating lidar. The TI has been computed accordingly and TI scatter plots have been color coded for the SV value.

To begin with the analysis, Fig. 13a shows the 10-min TI scatter plot and pertinent regression analysis when no filtering is applied (case (i)). As expected in this case, a comparatively poor correlation between the "reference"- and the "floating"-lidar TIs is found showing a comparatively poor determination coefficient ($\rho^2 = 0.885$) and a large offset term (slope, $m = 0.997$; offset, $n = -0.015$). The large offset is related to an overestimated TI caused by high-frequency motion-induced HWS fluctuations in the floating lidar. When addressing Fig. 13b (case (ii), window averaging) the determination coefficient and the offset terms are significantly enhanced ($\rho^2 = 0.911$, slope, $m = 1.011$; offset, $n = -6\ 10^{-4}$) but still several outliers broad the scatter plot. In more detail, and by using that each point is colored with its corresponding SV magnitude (refer to SV colorbar), we notice that most of these outliers correspond to high SV values ($SV > 0.1$). This $SV > 0.1$ relation translates into a 5% population when the 10-min histogram for the whole campaign is analysed.

Finally, Fig. 13c (case (iii), window averaging and SV filtering) shows one further improvement in the statistical indicators ($\rho^2 = 0.930$, slope, $m = 1.004$; offset, $n = -1\ 10^{-4}$) and a most relevant effect being the removal of the comparatively small population of SV outliers (5%) responsible for such high SV values ($SV > 0.1$). In summary, from case (i), i.e no filtering, to case (iii) the overall improvement in the statistical parameters goes from 0.996 to 1.003 in the slope; -0.0151 to -0.001 in the offset, and 0.885 to 0.930 in the determination coefficient. Overall, the latter represents a 5% enhancement factor in the TI determination coefficient (this figure can be taken as the percentage improvement achieved when estimating the TI from the floating lidar) while ensuring 95% data availability.

5. CONCLUSIONS

HWS and TI measurements at 100 m in height from a buoy Doppler lidar during a 38-day nearshore campaign at PdP (Badalona, Barcelona) have been revisited from a signal-processing methodology and statistical error-analysis perspective. This work has shown that *linear-fit indicators*, namely, slope, offset term and determination coefficient, and *time-series indicators*, namely, bias and RMSE, are useful error indicators to cross-examining "floating"- versus "reference"-lidar measurement datasets. 1-s time series analysis has enabled closer inspection of the HWS error behaviour, thus relating this error against angular motion amplitude of the floating lidar.

Study cases 1 and 2 (Sect. 4.2, Figs. 9, 10) have corroborated angular motion and lidar-observed wind turbulence (parameterized by the SV) as the main error sources affecting the floating lidar KPIs. At methodological level, daily HWS error histograms have been computed as a function of the floating-lidar angular-motion amplitude and SV. Though this histogram classification of the HWS error does not inherently guarantee perfect separation between error sources (i.e., the HWS error associated to a given angular-motion amplitude is always inherently measured under some level of SV) it has served to the purpose to identify these two dominant error sources, their behaviour, and in relation to the filtering methods presented.

Two filtering methods, adaptive window averaging and SV filtering have been proposed at post-processing level:

The window-averaging technique is implemented as a boxcar filter with an adaptive time window equal to the mean motion period (i.e., the inverse of angular-velocity spectrum peak frequency) recomputed on a 10-min basis. This technique has proven effective enough to minimize the impact of wave-induced angular motion on the floating lidar performance by yielding an overall improvement in all statistical indicators towards KPI compliance (Tab. II). Specifically, the default 30% 1-s KPI compliance when no filtering procedure is applied (case (i)) is raised to some 80% compliance when window averaging is applied (case (ii)). Likewise, when considering HWS results for the whole campaign (Sect. 4.4), the width of the 1-s HWS error histogram [44] is reduced from $\mathrm{RMSE_i} = 0.51$ m/s (12.24%, Tab. II) to $\mathrm{RMSE_{ii}} = 0.34$ m/s (7.39%, Tab. II). When considering TI (10-min data, Sect. 4.5), the offset between the "reference" and the "floating" lidar is reduced from $n_{\mathrm{i}} = -0.0157$ to $n_{\mathrm{ii}} = -6\ 10^{-4}$.

SV filtering, which is implemented as the SV threshold above which measurements are treated as outliers, represents a trade-off between KPI improvement and data availability. When both window averaging and SV filtering procedures are applied (case (iii)) 98% KPI compliance is achieved (70% 1-s data availability, $SV > 0.05$ threshold, Tab. II). Concerning TI (10-min data, Sect. 4.5) a further a 5% enhancement factor in the TI determination coefficient is obtained (95% data availability).

All in all, this work has enabled a wealth of signal processing and statistical methods to better understand the error behaviour of a ZephIR 300 floating Doppler wind lidar and ways to minimise these errors at post-processing level in relation to KPI compliance.

ACKNOWLEDGEMENT

This work has been funded by the European Institute of Innovation and Technology (EIT), KIC InnoEnergy project NEPTUNE (Offshore Metocean Data Measuring Equipment and Wind, Wave and Current Analysis and Forecasting Software, call 2011) with the participation of the Catalonia Institute for Energy Research (IREC, PI. coord. F. Schuon), Maritime Engineering Lab. of Universitat Politècnica de Catalunya (LIM-UPC, PI. D. González-Marco), Remote Sensing Lab. (RSLAB-UPC, PI. F. Rocadenbosch), University of Stuttgart (USTUTT, PI. O. Bischoff), Centro de Investigaciones Energéticas Medioambientales y Tecnológicas (CIEMAT, PI. A. Palomares), Gas Natural Fenosa (GNF, PI. R. Jané), and Soluciones de Ingeniería Marítima Operacional (SIMO, PI. F. Hermosilla), and by the Spanish Ministry of Economy and Competitiveness (MEC) - European Regional Development (FEDER) funds under TEC2015-63832 project. And, in part, by the European Union, FP7 ITN Marie Curie project, ITARS (Initial Training in Atmospheric Remote Sensing), GA-289923.

The authors gratefully acknowledge LIM-UPC for the development of the motion-simulator and cardanic frame devices and endless tests carried out at their premises as well as SWE-USTUTT at the initial stages of software development during the campaign. Two unknown reviewers are also acknowledged for the fruitful positive review comments to this paper.

REFERENCES

1. Arapogianni A, Pineda I, Moccia J. The european offshore wind industry - key trends and statistics 2012. *Technical Report*, The European Wind Energy Association January 2013.
2. Global Wind Energy Council. Global wind report annual market update 2013. *Technical Report*, Global Wind Energy Council April 2014.

3. Westerhellweg A, Canadillas B, Beeken A, Neumann T. One year of lidar measurements at fino1-platform: comparison and verification to met-mast data. *Proceedings of the 10th German Wind Energy Conference DEWEK 2010*, 2010.
4. Barthelmie RJ, Pryor SC. Can satellite sampling of offshore wind speeds realistically represent wind speed distributions? *Journal of Applied Meteorology* 2015/11/17 2003; **42**(1):83–94, doi:10.1175/1520-0450(2003)042⟨0083:CSSOOW⟩2.0.CO;2. URL http://dx.doi.org/10.1175/1520-0450(2003)042<0083:CSSOOW>2.0.CO;2.
5. Chang R, Zhu R, Badger M, Hasager CB, Zhou R, Ye D, Zhang X. Applicability of synthetic aperture radar wind retrievals on offshore wind resources assessment in hangzhou bay china. *Energies* 2014; .
6. Lavagnini A, Sempreviva AM, Barthelmie RJ. Estimating wind energy potential offshore in mediterranean areas. *Wind Energy* January 2003; .
7. Hirth BD, Schroeder JL, Gunter WS, Guynes JG. Measuring a utility-scale turbine wake using the ttuka mobile research radars. *Journal of Atmospheric and Oceanic Technology* 2012; .
8. Rodrigo JS. State-of-the-art of wind resource assessment. *Deliverable D7*, CENER 2010.
9. International Energy Association. State of the art of remote wind speed sensing techniques using sodar, lidar and satellites. *Technical Report*, International Energy Association January 2007.
10. Peña A, Hasager CB, Gryning SE, Courtney M, Antoniou I, Mikkelsen T. Offshore wind profiling using light detection and ranging measurements. *Wind Energy* 2009; **12**:105–124.
11. Pichugina YL, Banta RM, Brewer WA, Sandberg SP, Hardesty RM. Doppler lidar–based wind-profile measurement system for offshore wind-energy and other marine boundary layer applications. *Journal of Applied Meteorology and Climatology* February 2011; **51**:327–349.
12. Pryor S, Schoof JT, Barthelmie R. Empirical downscaling of wind speed probability distributions. *Journal of Geophysical Research: Atmospheres* 2005; **110**(D19).
13. Hasager CB, Nielsen M, Astrup P, Barthelmie R, Dellwik E, Jensen NO, Jørgensen BH, Pryor S, Rathmann O, Furevik B. Offshore wind resource estimation from satellite sar wind field maps. *Wind Energy* 2005; **8**(4):403–419.
14. Wolken-Möhlmann G, Lilov H, Lange B. Simulation of motion induced measurement errors for wind measurements using lidar on floating platforms. *Fraunhofer IWES, Am Seedeich* 2011; **45**:27 572.
15. Gottschall J, Wolken-Möhlmann G, Viergutz T, Lange B. Results and conclusions of a floating-lidar offshore test. *Energy Procedia* 2014; **53**:156 – 161.
16. Howe G. A floating lidar roadmap: Implications for offshore wind. *Technical Report*, AXYS Technologies Inc. 2014. URL http://axystechnologies.com/wp-content/uploads/2014/03/NACE_MarApr_2014_-AXYS.pdf.
17. Proceedings of the ASME 2013 32nd International Conference on Ocean O, OMAE2013 AE ((eds.)). *A low motion floating platform for offshore wind resource assessment using Lidars*, ASME, 2013.
18. Schuon F, González D, Rocadenbosch F, Bischoff O, Jané R. KIC InnoEnergy Project Neptune: Development of a Floating LiDAR Buoy for Wind, Wave and Current Measurements. *Proceedings DEWEK 2012 German Wind Energy Conference*, DEWI, 2012.
19. M Pitter EBdR, Medley J, Mangat M, Slinger C, Harris M. Performance stability of zephir in high motion enviroments: floating and turbine mounted. *Technical Report*, Zephir 2014.
20. Carbon Trust. Carbon trust offshore wind accelerator roadmap for the commercial acceptance of floating lidar technology. *Technical Report*, Carbon Trust November 2013.
21. Tiana-Alsina J, Gutiérrez MA, Würth I, Puigdefàbregas J, Rocadenbosch F. Motion compensation study for a floating doppler wind lidar. *Geoscience and Remote Sensing Symposium Proceedings*.
22. Gottschall J, Lilov H, Wolken-Möhlmann G, Lange B. Lidars on floating offshore platforms; about the correction of motion-induced lidar measurement errors. *EWEA 2012 proceedings*, 2012 E (ed.), 2012.
23. Courtney MS, Hasager CB. *Remote sensing technologies for measuring offshore wind*, chap. 4. 2016; 59–82.
24. Proakis JG, Manolakis DK. *Digital Signal Processing (4th Edition)*. Prentice-Hall, Inc.: Upper Saddle River, NJ, USA, 2006.
25. Sathe A, Mann J, Gottschall J, Courtney M. Can wind lidars measure turbulence? *Journal of Atmospheric and Oceanic Technology* 2011; **28**(7):853–868.
26. Gottschall J, Courtney M, Wagner R, Jørgensen HE, Antoniou I. Lidar profilers in the context of wind energy–a verification procedure for traceable measurements. *Wind Energy* 2012; **15**(1):147–159.
27. Cool GA. Floating lidar technology. oceanographic parameters influencing accuary of wind vector reconstruction. Master's Thesis, Aerospace Eng., Delf University of Technology September 2016.
28. Sospedra J, Cateura J, Puigdefabregas J. Novel multipurpose buoy for offshore wind profile measurements. *Sea Technology* 2015; .
29. Mangat M. Repeatability of zephir 300 performance. *Technical Report*, ZephIR Lidar 2016.

30. Henderson SW, Gatt P, Rees D, Huffaker M. *Laser Remote Sensing, Chapter 7: Wind LIDAR*. Optical Science and Engineering, CRC Press, 2005.
31. Wharton S, Lundquist JK. Assessing atmospheric stability and its impacts on rotor-disk wind characteristics at an onshore windfarm. *Wind Energy* 2012; **15**(4):525–546, doi:10.1002/we.483. URL http://dx.doi.org/10.1002/we.483.
32. Nino R, Eecen P. Turbulence and wind shear: a literature study and measurements. *ECN, Petten* 2001; .
33. Sjöholm M, Mikkelsen TK, Kristensen L, Mann J, Kirkegaard P. Spectral analysis of wind turbulence measured by a doppler lidar for velocity fine structure and coherence studies. *In Detailed Program (online)*. 2010.
34. Wagner R, Mikkelsen T, Courtney M. Investigation of turbulence measurements with a continuous wave, conically scanning lidar. *Technical Report*, DTU March 2009.
35. Taylor GI. The spectrum of turbulence. *Proceedings of the Royal Society of London. Series A, Mathematical and Physical Sciences* 1938; **164**(919):476 – 490.
36. Belu R, Koracin D. Statistical and spectral analysis of wind characteristics relevant to wind energy assessment using tower measurements in complex terrain. *Journal of Wind Energy* 2013; :12doi:10.1155/2013/739162. URL http://dx.doi.org/10.1155/2013/739162.
37. Bischoff O, Schlipf D, Würth I, Cheng P. Dynamic motion effects and compensation methods of a floating lidar buoy. *EERA DeepWind 2015 Deep Sea Offshore Wind Conference*, EERA (ed.), 2015.
38. ARFKEN G. INTRODUCTION. *Mathematical Methods for Physicists*. Elsevier BV, 1985; xxi–xxii, doi:10.1016/b978-0-12-059820-5.50008-2. URL http://dx.doi.org/10.1016/b978-0-12-059820-5.50008-2.
39. Schlipf D, Rettenmeier A, Haizmann F, Hofsäß M, Courtney M, Cheng PW. Model based wind vector field reconstruction from lidar data. *Proceedings of the 11th German Wind Energy Conference DEWEK 2012*, 2012.
40. Arranz PG. Measurements in complex terrain using a lidar. *Technical Report*, CENER February 2011.
41. Barlow RJ. *Statistics: a guide to the use of statistical methods in the physical sciences*. Manchester physics series, Wiley: Chichester, 1989. URL https://cds.cern.ch/record/213033.
42. Canadillas B, Bégué A, Neumann T. Comparison of turbulence spectra derived from lidar and sonic measurements at the offshore platform fino1. *Proceedings DEWEK 2010 German Wind Energy Conference*, DEWI, 2010.
43. Frisch U. *Turbulence: The Legacy of AN Kolmogorov*. Cambridge University Press, 1995.
44. Gutiérrez MA, Tiana-Alsina J, Bischoff O, Cateura J, Rocadenbosch F. Performance evaluation of a floating doppler wind lidar buoy in mediterranean near-shore conditions. *Geoscience and Remote Sensing Symposium Proceedings*.

Table I. 1-s and 10-min KPIs (adapted from [20]).

KPI	Acceptance criteria (1-s)	Acceptance criteria (10-min)
Mean HWS slope, m	0.96-1.04	0.98-1.02
Mean HWS offset, n	$< 3\% \cdot v_{ref,mean}$ [m/s]	$< 4\% \cdot v_{ref,mean}$ [m/s]*
Mean HWS coefficient of determination, ρ^2	> 0.95	> 0.98
Mean HWS Bias	$< 5\% \cdot v_{ref,mean}$ [m/s]	$< 4\% \cdot v_{ref,mean}$ [m/s]*
Mean HWS RMSE	$< 8\% \cdot v_{ref,mean}$ [m/s]	$< 4\% \cdot v_{ref,mean}$ [m/s]*
Mean WD slope, m	0.97-1.03	0.97-1.03
Mean WD offset, n	< 5 [deg]	< 5 [deg]
Mean WD coefficient of determination, ρ^2	> 0.95	> 0.97

Table II. 1-s and 10-min error-assessment indicators for the whole PdP campaign.

	ρ^2	slope	Offset	bias	RMSE
1-s data					
HWS (case i)	0.926	0.953	4.69%	2.34%	12.24%
HWS (case ii)	0.969	0.993	1.56%	0.68%	7.39%
HWS (case iii)	0.981	0.995	1.38%	0.62%	5.44%
10-min data					
HWS (case i)	0.996	1.005	0.10%	0.29%	3.43%
HWS (case iii)	0.996	1.005	0.10%	0.29%	3.43%
TI (case i)	0.886	0.997	15.75%	15.50%	23.60%
TI (case ii)	0.911	1.010	0.62%	0.50%	20.84%
TI (case iii)	0.929	1.000	0.65%	0.68%	18.03%